Nano Research 2018, 11(6): 3294–3305
https://doi.org/10.1007/s12274-017-1874-y
Research Article
ISSN 1998-0124
CN 11-5974/O4

Coordination-responsive drug release inside gold nanorod@metal-organic framework core–shell nanostructures for near-infrared-induced synergistic chemo-photothermal therapy

Yantao Li[§], Jun Jin[§], Dawei Wang, Jiawei Lv, Ke Hou, Yaling Liu (✉), Chunying Chen (✉), and Zhiyong Tang (✉)

CAS Key Laboratory of Nanosystem and Hierarchical Fabrication, CAS Center for Excellence in Nanoscience, National Center for Nanoscience and Technology, Beijing 100190, China
[§]Yantao Li and Jun Jin contributed equally to this work.

Received: 8 August 2017
Revised: 30 September 2017
Accepted: 1 October 2017

© Tsinghua University Press and Springer-Verlag GmbH Germany 2017

KEYWORDS
core–shell nanostructures,
coordination bonds,
dual stimuli response,
synergistic cancer therapy

ABSTRACT

Multifunctional core–shell nanostructures formed by integration of distinct components have received wide attention as promising biological platforms in recent years. In this work, crystalline zeolitic imidazolate framework-8 (ZIF-8), a typical metal-organic framework (MOF), is coated onto single gold nanorod (AuNR) core for successful realization of synergistic photothermal and chemotherapy triggered by near-infrared (NIR) light. Impressively, high doxorubicin hydrochloride (DOX) loading capacity followed by pH and NIR light dual stimuli-responsive DOX release can be easily implemented through formation and breakage of coordination bonds in the system. Moreover, under NIR laser irradiation at 808 nm, these novel AuNR@MOF core–shell nanostructures exhibit effective synergistic chemo-photothermal therapy both *in vitro* and *in vivo*, confirmed by cell treatment and tumor ablation via intravenous injection.

Cancer therapy, one of the major solutions to improve human health, has remained a tremendous challenge even though great efforts have been devoted to cancer research [1–4]. Essentially, many types of cancer treatments including surgery, radiation therapy, immunotherapy, and hyperthermia treatment have been broadly performed. However, as an individual monotherapy, all of them show severe limitations including adverse side effects, symptoms of nausea and emesis, anxiety related to chemotherapy, and non-specific damage to healthy cells [5, 6]. Therefore, in order to overcome the inherent limitations of the single-treatment modality and further satisfy the growing demand for efficient treatment, the design of a multifunctional nanoplatform that can combine different therapeutic modalities to synergistically address diseases has become the mainstream in cancer therapy [7, 8]. Many nanostructured systems

Address correspondence to Yaling Liu, liuyl@nanoctr.cn; Chunying Chen, chenchy@nanoctr.cn; Zhiyong Tang, zytang@nanoctr.cn

composed of different functional units have been designed and employed for high-performance cancer therapy, among which core–shell nanostructures have received special interest owing to the facile and accurate control over the size, shape, structure, and function of both components [9, 10]. Evidently, selection of suitable constituent materials is of vital importance to the development of core–shell nanostructures with improved therapeutic efficacy and reduced side effects.

Noble metal nanoparticles (NPs), especially anisotropic gold NPs (AuNPs), are broadly recognized as intriguing candidates for cancer theranostics because of their good biocompatibility, high light-to-heat conversion efficiency, and unique near-infrared (NIR) light adsorption feature [11–14]. Notably, NIR light is known to show low absorption and deep penetration in tissues, and is considered as a promising source for effective disease treatment while minimizing side effects [15, 16]. Hence, anisotropic AuNPs with NIR-light-triggered photothermal properties are one of the ideal constituent units for construction of multimodal treatment systems, among which the core–shell structures are mostly adopted. For example, when AuNPs are used as the cores in drug delivery systems, light-to-heat conversion of AuNPs can stimulate on-demand drug release from the shell materials for site-specific cancer chemotherapy [17, 18]. Unfortunately, all currently reported core–shell nanostructures based on AuNPs for cancer therapy have their own deficiencies, likely because of the property restriction of the shell materials upon controlled drug release in response to internal or external triggers. For instance, the limited drug-loading capacity and instability of organic shell materials such as liposomes, polymers, and dendrimers make controlled drug release inefficient, especially under NIR light excitation [19, 20]. By contrast, inorganic shell materials such as mesoporous silica (a typically inert drug carrier) might be good at controllable drug release while conjugated to activated nanovalves or pH-responsive groups [21, 22]. However, most of these systems have poor biodegradability and need complicate synthesis via graft-from strategies with toxic catalysts. Therefore, in order to break through the application limitations of current AuNP-based treatment systems, it is imperative to discover new types of shell materials for highly efficient cancer therapy.

Metal-organic frameworks (MOFs), which are typical inorganic–organic hybrid materials composed of metal ions or clusters bridged by organic linkers, have emerged as a promising platform in biomedical applications owing to their high tenability of composition and structure, easy functionalization, good biocompatibility, and intrinsic biodegradability [23–26]. It is noteworthy that both bulk MOFs and nanoscale MOFs (NMOFs) have exhibited many intriguing characteristics as drug carriers, such as exceptionally high surface areas and large pore sizes for drug loading as well as versatile interactions (van der Waals forces, π–π stacking, hydrogen bonds, electrostatic forces, or coordination bonds) for drug adsorption [27–29]. More importantly, their versatile structures endow MOFs with multifunctionalities and offer the opportunity for stimuli-responsive drug release. A variety of stimuli-responsive MOFs, including single-stimulus-responsive MOFs and multiple-stimuli-responsive MOFs, have been reported for regulated delivery of loaded drugs upon activation by diverse stimuli, e.g., pH, magnetic field, ions, temperature, light, and pressure, demonstrating that MOFs are appealing candidates for the construction of multimodal treatment systems with controllable drug release [30–35]. Among them, crystalline zeolitic imidazolate framework-8 (ZIF-8), a classical MOF formed by coordination interaction between low-toxicity Zn^{2+} and 2-methylimidazole (2-MIM), holds an intersecting three-dimensional structure of guest-matching pore size and large surface area, enabling considerable increase of drug-loading amount and easy surface modification [36, 37]. Consequently, a series of multifunctional core–shell NPs@ZIF-8 nanostructures including polyacrylic acid@ZIF-8, CuS@ZIF-8, and graphene quantum dot@ZIF-8 [38–40], have received much attention as advanced functional nanomaterials for theranostics. However, for all currently reported NPs@ZIF-8, only some of the applications similar to those of SiO_2 or polymeric shell materials, such as high drug loading, pH-responsive release, multimodal imaging, and cancer therapy, have been demonstrated. Nevertheless, the unique advantages of ZIF-8 as shells have not been revealed, and there are no reports on synergistic cancer therapy based on NPs@ZIF-8 *in*

vivo under NIR irradiation, which enables great potential development of NPs@MOF nanomaterials in biomedicine.

Herein, we combine AuNPs and ZIF-8 into core–shell nanostructures to fully reveal the distinct features and mechanism of AuNPs@ZIF-8 as a multifunctional nanoplatform for improved multimodal cancer therapy and even *in vivo* bioapplications, especially under NIR irradiation. In detail, ZIF-8 was coated onto the core of a single gold nanorod (AuNR) for successful realization of synergistic photothermal and chemotherapy triggered by NIR light. Compared with spherical AuNPs, anisotropic AuNRs possess additional strong longitude surface plasmon resonance (LSPR) adsorption characteristic in the NIR region, allowing deeper tissue penetration and endowing the opportunity to achieve controlled drug release [41, 42]. Furthermore, *in vivo* fate can be controlled by the ZIF-8 shell via drug loading and response to stimuli. Thus, as-fabricated AuNR@ZIF-8 core–shell nanostructures exhibit high doxorubicin hydrochloride (DOX)-loading capacity followed by pH and NIR light dual stimuli-responsive DOX release, which is realized through the formation and breakage of coordination bonds between metallic and organic active sites in the system that are seldom reported in SiO_2 or polymeric shell materials. Significantly, the AuNR@ZIF-8 core–shell nanostructures display low systemic toxicity, remarkable biocompatibility, and good biodegradation. Under NIR laser irradiation at 808 nm, two synergistic modes, namely manageable photothermal effect and dual stimuli-responsive (heat and pH) drug release, work together for high-performance cancer therapy both *in vitro* and *in vivo*, the mechanism of which is also fully revealed. More importantly, these results have been confirmed by both cell treatment and tumor ablation via intravenous injection.

The AuNR@ZIF-8 core–shell nanostructures were synthesized according to the strategy shown in Scheme 1. First, cetyltrimethylammonium bromide (CTAB)-stabilized AuNRs with an average diameter and length of 47 nm and 12 nm, respectively, were pre-prepared using the seed-mediated method (Fig. 1(a) and Fig. S1 in the Electronic Supplementary Material (ESM)) [43]. Figure S1(b) in the ESM shows that as-synthesized AuNRs had a strong LSPR peak at ~ 790 nm. Subsequently, the CTAB stabilizers on the AuNR surfaces were exchanged with polyvinylpyrrolidone (PVP) considering the possible toxicity of cationic CTAB on cells and tissues as well as good binding of PVP toward AuNRs (Fig. S2(a) in the ESM) [44–46]. Then, 2-MIM was homogeneously mixed with the PVP-stabilized AuNRs by gentle stirring. After that, a solution of $Zn(NO_3)_2{\cdot}6H_2O$ in methanol was added into the mixed solution, and after 2 min, the products of the core–shell nanostructures could be discerned (Fig. S2(b) in the ESM). As the reaction continued, the ZIF-8 shell gradually stacked and self-grew to become thick (Fig. S2(c) and Fig. S2(d) in the ESM) and finally monodisperse AuNR@ZIF-8 core–shell nanostructures with an average size of ~ 140 nm were obtained (Fig. 1(b) and Fig. S3 in the ESM). The high-angle annular dark-field scanning transmission electron microscopy (HAADF-STEM) image clearly indicates that the products had a typical core–shell structure (Fig. 1(c)), and energy-dispersive X-ray (EDX) elemental mapping further shows that Au was located only at the core while C, N, and Zn of ZIF-8 were homogeneously distributed within the entire nanostructure (Fig. 1(d)), revealing that single AuNR core was surrounded by a uniform ZIF-8 shell.

In addition to morphology characterization, crystal structure analysis based on powder X-ray diffraction (XRD) pattern indicates that the core–shell products

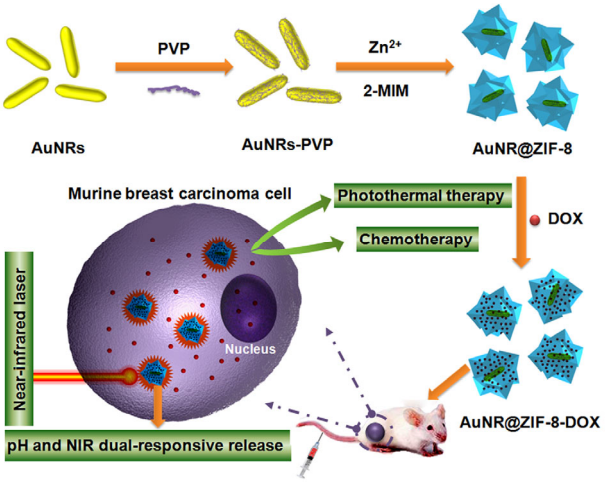

Scheme 1 Strategy for fabrication of AuNR@ZIF-8 core–shell nanostructures as a novel multifunctional nanoplatform for synergistic chemo-photothermal cancer therapy both *in vitro* and *in vivo*.

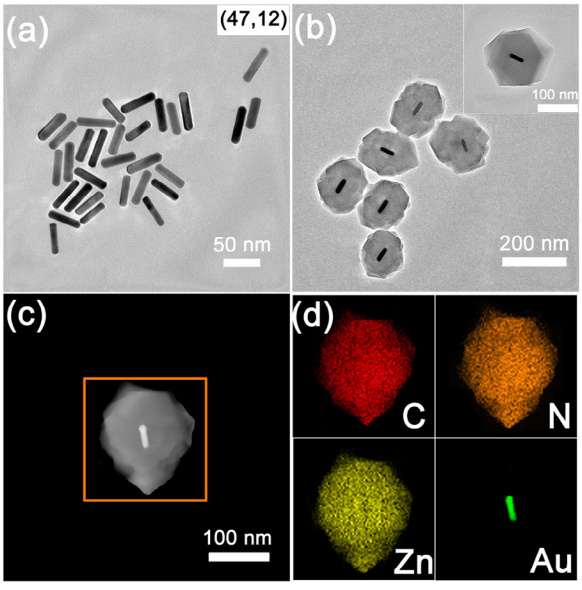

Figure 1 (a) TEM image of CTAB-stabilized AuNRs. The number in brackets represents the average length and diameter (in nanometers) of AuNRs determined by statistical data; (b) TEM image of AuNR@ZIF-8 core–shell nanostructures; (c) HAADF-STEM image of single AuNR@ZIF-8 core–shell nanostructure; (d) EDX elemental mapping of one AuNR@ZIF-8 core–shell nanostructure marked in (c).

possess two sets of characteristic peaks (black curve in Fig. 2(a)). Such a pattern corresponds to face-centered cubic Au at high angles of 35°–90° and cubic crystalline ZIF-8 at low angles of 3°–35° that well match the theoretical powder pattern of ZIF-8 (red curve in Fig. 2(a)). No other peaks assigned to impurities are observed. Importantly, further XRD patterns confirm that the AuNR@ZIF-8 core–shell nanostructures exhibited good stability in phosphate buffered saline (PBS) solution even after 7 days of immersion, which is conducive to their further biological applications (Fig. S3(e) in the ESM). Moreover, Brunauer–Emmett–Teller (BET) measurement was performed to determine the porosity of the AuNR@ZIF-8 core–shell nanostructures (red curve in Fig. 2(b) and Fig. S4(d) in the ESM). The N_2 adsorption–desorption isotherm for the AuNR@ZIF-8 core–shell nanostructures displays a typical type I curve, disclosing that the structure was mainly micro-porous [47]. The BET surface area of the AuNR@ZIF-8 core–shell nanostructures was calculated to be 1,130.5 $m^2 \cdot g^{-1}$, which is considerably lower than 1,664.4 $m^2 \cdot g^{-1}$ of pure ZIF-8 nanocrystals prepared under similar condition (black curve in Fig. 2(b) and Fig. S4 in the ESM). The reduced surface area is reasonable considering the contribution of solid AuNR cores to the total mass of the AuNR@ZIF-8 core–shell nanostructures. Nevertheless, the pore size and pore volume of the AuNR@ZIF-8 core–shell nanostructures (1.74 nm and 0.82 $cm^3 \cdot g^{-1}$) are higher than those of pure ZIF-8 nanocrystals (1.15 nm and 0.68 $cm^3 \cdot g^{-1}$) (Table S1 in the ESM). Particularly, considerable mesopores (4–9 nm, shown in the inset of Fig. S4(d) in the ESM) appeared within the ZIF-8 shells due to multidomain growth of the ZIF-8 shells around the AuNR cores (Fig. S2 in the ESM) [43, 44], which greatly benefits the AuNR@ZIF-8 core–shell nanostructures as promising high-loading drug nanocarriers, especially for large-sized drug molecules [33].

In order to evaluate the AuNR@ZIF-8 core–shell nanostructures as therapeutic agents, their optical properties and corresponding photothermal effect

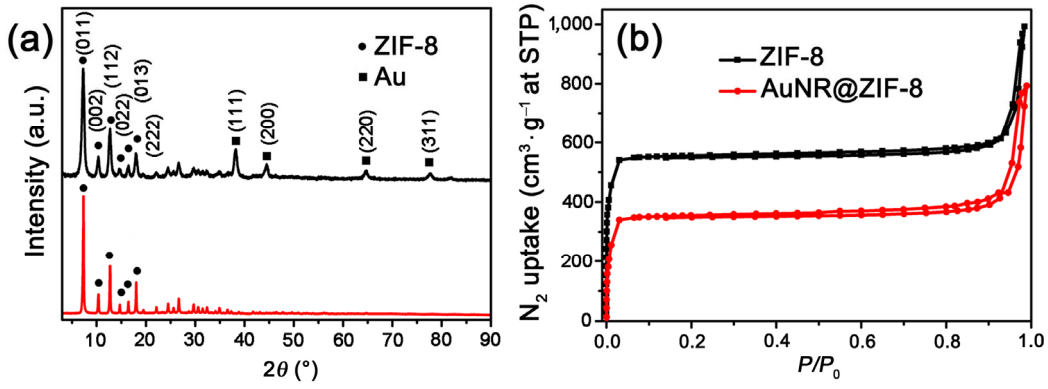

Figure 2 (a) XRD patterns of AuNR@ZIF-8 core–shell nanostructures (black curve) and simulated ZIF-8 crystals (red curve); (b) N_2 adsorption/desorption isotherms of AuNR@ZIF-8 core–shell nanostructures and pure ZIF-8 nanocrystals.

were first investigated. As seen from Fig. S5(a) in the ESM, the AuNR@ZIF-8 core–shell nanostructures show a broad LSPR absorption centered at ~ 810 nm, presenting a small bathochromic shift (~ 20 nm) compared with that of pure AuNRs due to coating of the ZIF-8 shells (Fig. S1(b) in the ESM), which is consistent with the previously reported theoretical result [21]. It is noticed that protection of the porous ZIF-8 shells prevents clustering and aggregation of the core–shell nanostructures in the solution, so the position of the LSPR band of AuNR cores in the NIR window does not exhibit a large shift. Subsequently, the 808-nm NIR laser (1 W·cm^{-2}) was selected as the excitation source to heat the AuNR@ZIF-8 core–shell nanostructures. As displayed in Fig. 3(a), it is evident that the AuNR@ZIF-8 core–shell nanostructures exhibited significant photothermal effect. The temperature of the PBS solution containing the AuNR@ZIF-8 core–shell nanostructures (0.1 mg·mL^{-1}) rapidly increased from room temperature (25.0 ˚C) to 50.4 ˚C within 5 min of NIR irradiation (red curve in Fig. 3(a)), which was expected to result in irreversible damage to tumor cells. In comparison, the temperature of PBS solution only slightly rose to 30.3 ˚C within 5 min of NIR irradiation (green curve in Fig. 3(a)). More interestingly, the solution temperature is easily tuned by either changing the concentration of the AuNR@ZIF-8 core–shell nanostructures or adjusting the power of the NIR laser (Fig. 3(a) and Fig. S6 in the ESM), which would meet various temperature requirements for cancer therapy.

A typical model anticancer drug, DOX, was selected to examine the drug-loading capacity of the AuNR@ZIF-8 core–shell nanostructures. The loading of DOX into the AuNR@ZIF-8 core–shell nanostructures was performed through simple mixing in aqueous solution at room temperature. With time, the color of the mixed solution changed from gray to purple (Fig. S5(c) in the ESM), suggesting the successful loading of DOX into the AuNR@ZIF-8 core–shell nanostructures (denoted as AuNR@ZIF-8-DOX complexes) via formation of transition metal-DOX complexation [48].

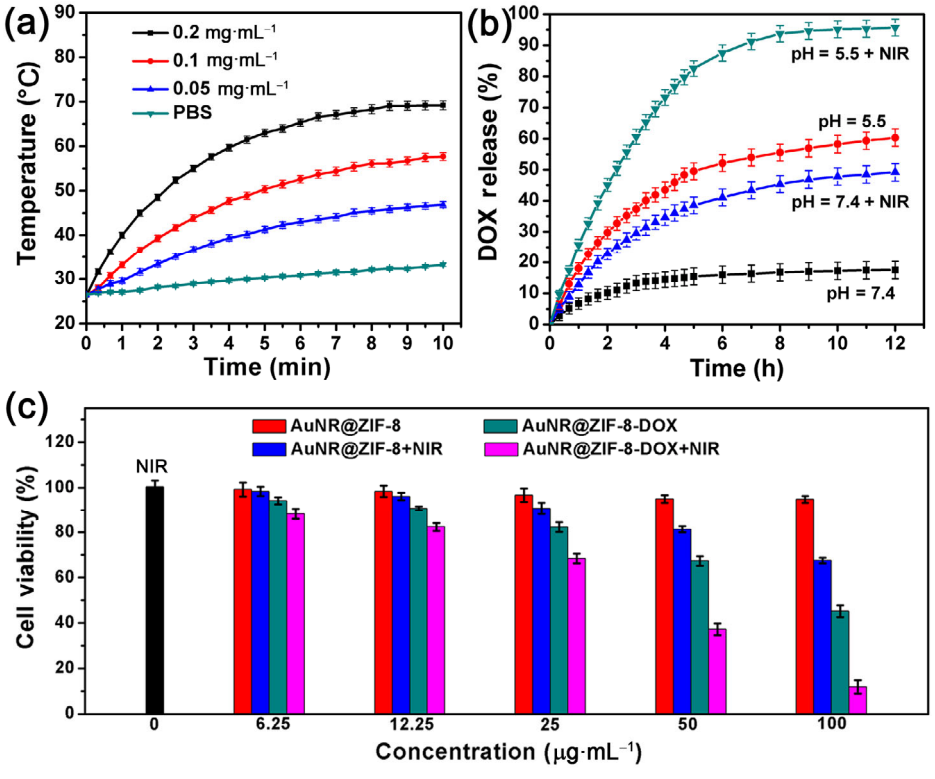

Figure 3 (a) Concentration-dependent temperature increase of AuNR@ZIF-8 core–shell nanostructures in PBS solution under NIR laser irradiation (1 W·cm^{-2}). Pure PBS solution (pH = 7.4) was used as negative control; (b) DOX release profiles from AuNR@ZIF-8-DOX complexes with and without NIR laser irradiation at different pH values; (c) CCK-8 assay of $4T_1$ cells with different treatments.

EDX elemental mapping survey further disclosed that DOX molecules were homogeneously loaded into the entire nanostructures (Fig. S7(b) in the ESM). Similarly, as shown in the Fourier transform infrared spectrum of the AuNR@ZIF-8-DOX complexes, the appearance of the $-NH_2$ stretching vibration at 3,441 cm^{-1} and the skeletal vibration of DOX molecules at 1,286 cm^{-1} reveals that DOX molecules were incorporated into the core–shell nanostructures (Fig. S7(c) in the ESM) [49]. Meanwhile, the obvious shift and broadening of the stretching vibration of three C=O groups, one at 1,725 cm^{-1} assigned to carboxylic acid and two others at 1,613 and 1,583 cm^{-1} attributed to carbonyl in anthracene ring, denotes the formation of coordination bonds between the C=O groups of DOX molecules and Zn^{2+} ions in the ZIF-8 shells (Fig. S7(c) in the ESM) [40, 49]. Corresponding molecular docking simulation also confirmed that DOX molecules were mainly bonded onto ZIF-8 via interaction of oxygen in both anthracene ring and carboxyl acid with Zn^{2+} ions [50]. Furthermore, the loading content of DOX could be quantitatively calculated based on the ultraviolet–visible (UV–Vis) absorption spectra (Fig. S5(b) in the ESM). By varying the weight ratio between DOX and the AuNR@ZIF-8 core–shell nanostructures, the loading content could reach ~ 0.358 mg of DOX per 1 mg of AuNR@ZIF-8 core–shell nanostructures (Table S2 in the ESM), which is comparable to previously reported nanocarriers of Au@SiO_2, Au@polymer, NMOFs, or NPs@NMOFs with high loading content [33, 51–56]. Importantly, neither size increase nor dissociation of the core–shell nanostructures was discerned after DOX loading (Fig. S8(b) in the ESM), manifesting the good stability of the AuNR@ZIF-8 core–shell nanostructures during the drug-loading process.

Both pH and NIR light are effective tools to control the release of AuNR@ZIF-8-DOX complexes. First, *in vitro* drug release experiments were carried out in PBS solutions at different pH values (5.5 and 7.4) without NIR irradiation. As shown in Fig. 3(b), the drug release rate in solution at pH 5.5 was obviously faster than that in solution at pH 7.4. After 12 h, the cumulative release of DOX in solution at pH 5.5 was ~ 60% and much higher than ~ 17% in solution at pH 7.4 [57]. Acidic conditions are beneficial to drug release because of pH-sensitive binding of both Zn–O between DOX and ZIF-8, and Zn–N between Zn^{2+} and imidazolate. In addition, the breakage of Zn–O and Zn–N coordination bonds triggered by low pH promotes the rapid release of DOX molecules [33, 49]. TEM imaging (Figs. S8(c) and S8(d) in the ESM) and inductively coupled plasma mass spectroscopy (Fig. S9 in the ESM) indicate that partial ZIF-8 shells were disassembled under acidic condition (pH = 5.5) whereas ZIF-8 shells were rather stable under physicological condition (pH = 7.4) [37, 53, 58].

In order to clarify the effect of NIR light on controlled drug release, AuNR@ZIF-8-DOX complexes in PBS solutions at pH 7.4 were irradiated by an NIR laser at 808 nm, which resulted in an increase in the solution temperature to 50 °C by adjusting the power of NIR laser. After 12 h, the cumulative release of DOX (~ 50%) was nearly 3 times higher than that in PBS solution at pH 7.4 without NIR irradiation. In view of the good stability of ZIF-8 in solution at pH 7.4 even at 50 °C [59], the enhanced DOX release for the system at pH 7.4 under NIR irradiation was mainly attributed to the NIR light-converted heat that makes dissociation of the Zn–O coordination bonds between DOX and ZIF-8 easier [39, 53, 54]. Furthermore, AuNR@ZIF-8-DOX complexes in PBS solution at pH 5.5 were also irradiated by an NIR laser at 808 nm. Significantly, after 12 h, the cumulative release of DOX reached ~ 95%. At the lower pH value mentioned above, the strength of the coordination bonds within AuNR@ZIF-8-DOX complexes (including the Zn–O and Zn–N coordination bonds) could decrease greatly with temperature increment [60]. Then, the enormously enhanced cumulative DOX release at pH 5.5 with NIR irradiation was mainly attributed to the much easier breakage of Zn–O and Zn–N coordination bonds with temperature increment caused by light-converted heat at lower pH. Correspondingly, irradiation of NIR laser combined with the acidic condition (pH = 5.5) caused the ZIF-8 shells to be severely dissembled (Fig. S8(f) in the ESM) and ~ 70% of zinc ions were released, which is about 2.1-fold higher than that in solution at pH 5.5 without NIR irradiation and 23.3-fold higher than that in solution at

pH 7.4 without NIR irradiation (Fig. S9 in the ESM). It should be mentioned that localized heating on the DOX-loaded AuNR@ZIF-8 nanostructures induced by NIR irradiation is crucial for quick drug release [39]. When AuNR@ZIF-8-DOX complexes are irradiated by NIR laser, both the low coefficients of NIR-light absorption and thermal conductivity of the ZIF-8 shells (0.165–0.19 $W \cdot m^{-1} \cdot K^{-1}$, much lower than 0.61–0.68 $W \cdot m^{-1} \cdot K^{-1}$ of water at 50 ˚C) give rise to fast attenuation of NIR-converted heat away from the AuNR cores (left image in Fig. S10(a) in the ESM) [61–64]. In view of maintaining the temperature of the entire drug release system at ~ 50 ˚C, the high efficiency of NIR-converted heat caused by AuNRs can cause the temperature around the AuNR cores to be much higher than 50 ˚C [62], leading to faster breakage of coordination bonds in the ZIF-8 shells followed by easier disassembly of the ZIF-8 shells and improved drug release. The control experiment of directly heating the PBS solution of AuNR@ZIF-8-DOX complexes (pH = 5.5) using an oil bath further confirms that with homogeneous thermal distribution, both the cumulative release of DOX (~ 76% after 12 h, Fig. S10(b) in the ESM) and the disassembled amount of zinc ions (~ 48%, Fig. S9 in the ESM) were obviously lower than those under NIR irradiation.

Altogether, the high drug-loading capacity as well as pH- and NIR-controlled drug release of the AuNR@ZIF-8 core–shell nanostructures were easily realized through forming and breaking coordination bonds between metallic and organic active sites without any complicated process of synthesis or modification. These features make the AuNR@ZIF-8 core–shell nanostructures promising as drug nanocarriers with site-specific controlled release of high-dose drugs for efficient cancer therapy, which is particularly important for future *in vivo* experiments.

To further evaluate the feasibility of the AuNR@ZIF-8 core–shell nanostructures for cancer therapy, the cytotoxicity of the AuNR@ZIF-8 core–shell nanostructures with and without DOX loading was analyzed by CCK-8 assay and confocal imaging on the murine breast carcinoma cell line $4T_1$ in the dark or under NIR laser irradiation at 808 nm (1 $W \cdot cm^{-2}$). As shown in Fig. 3(c), the viability of $4T_1$ cells incubated with the AuNR@ZIF-8 core-shell nanostructures without DOX (red bars) was almost the same as that of the control group (cells incubated without any nanostructure under NIR irradiation), demonstrating the excellent biocompatibility and negligible cytotoxicity of the AuNR@ZIF-8 core–shell nanostructures. With the elevated concentration of AuNR@ZIF-8 core-shell nanostructures, increased death of tumor cells incubated with the AuNR@ZIF-8 core–shell nanostructures under NIR laser irradiation (blue bars) or with AuNR@ZIF-8-DOX complexes without NIR irradiation (green bars) could be observed obviously, confirming that the AuNR@ZIF-8 core–shell nanostructures provide two different therapeutic modes for cancer therapy: photothermal therapy under NIR irradiation and chemotherapy through DOX release. When the cells were incubated with AuNR@ZIF-8-DOX complexes under irradiation by NIR laser at 808 nm, the highest cell mortality was achieved (purple bars). When the concentration of the AuNR@ZIF-8-DOX complexes was 100 $\mu g \cdot mL^{-1}$, approximately 90% of $4T_1$ cells were killed, which was much more effective in comparison to AuNR@ZIF-8-DOX complexes at 100 $\mu g \cdot mL^{-1}$ without NIR irradiation (~ 55% cell death) or AuNR@ZIF-8 core–shell nanostructures at 100 $\mu g \cdot mL^{-1}$ under NIR irradiation (~ 33% cell death). Evidently, the AuNR@ZIF-8 core–shell nanostructures would be a powerful platform for combined chemo-photothermal therapy with excellent synergy.

The combined therapeutic effect of the AuNR@ZIF-8 core–shell nanostructures was also investigated with Calcein-AM (green)/propidium iodide (red) double staining, which is a popular method to evaluate photothermal chemotherapeutic effect after treatment with DOX-containing carriers [21, 65, 66]. After incubation with either AuNR@ZIF-8 core–shell nanostructures or AuNR@ZIF-8-DOX complexes for 12 h, $4T_1$ cells were subjected to NIR laser irradiation at 808 nm for 5 min, and then cultured normally for the next 0 h and 24 h at 37 ˚C in the dark. As displayed in Fig. 4(a), with respect to the blank $4T_1$ cells, NIR laser irradiation for 5 min did not give rise to cell death in the following 24 h of culture. In the case of $4T_1$ cells incubated with the AuNR@ZIF-8 core–shell nanostructures, there was some cell death to be distinguished after 5 min of irradiation in the following 24 h of culture (Fig. 4(b3)), which was

caused by the photothermal effect of the AuNR@ZIF-8 core–shell nanostructures. In comparison, incubation

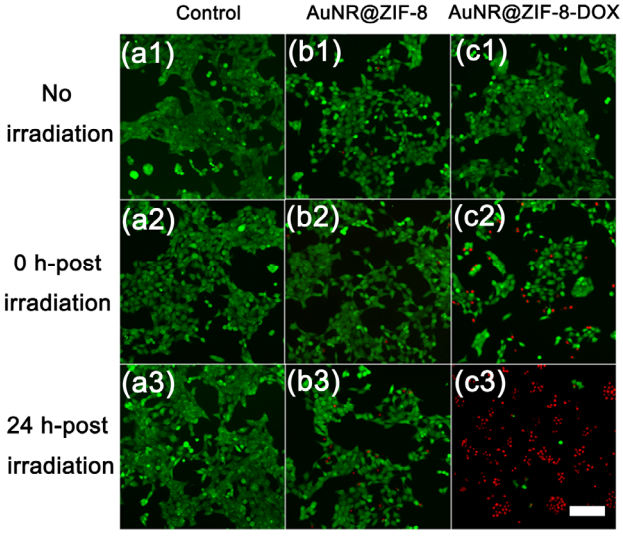

Figure 4 NIR-light-triggered DOX release within $4T_1$ cells and its influence on cell viability. The effect on lysosomal membrane integrity was determined by Calcein-AM (green)/propidium iodide (red) double staining. Confocal images of (a) blank $4T_1$ cells; (b) $4T_1$ cells incubated with AuNR@ZIF-8 core–shell nanostructures; (c) $4T_1$ cells incubated with AuNR@ZIF-8-DOX complexes. Row 1: crude samples; Row 2: samples irradiated by NIR laser for 5 min; Row 3: samples irradiated for 5 min after 24 h of culture. Scale bar: 100 μm.

with the AuNR@ZIF-8-DOX complexes caused a sharp increase in cell death at 24 h after 5 min of irradiation (Fig. 4(c3)), which was attributed to the combined photothermal and chemotherapeutic effect. These results are in good agreement with those from the CCK-8 assay (Fig. 3(c)), collectively confirming that the AuNR@ZIF-8-DOX complexes can be effectively applied to destroy cancer cells with combined photothermal and chemotherapy. Furthermore, cellular uptake experiments confirmed the potential of the high antitumor efficacy of AuNR@ZIF-8-DOX complexes by analyzing their location after cell internalization (Fig. S11 in the ESM).

Tumor-bearing mice prepared by implanting 1×10^6 $4T_1$ cells at their right hind legs were used to evaluate the *in vivo* therapeutic efficacy of the AuNR@ZIF-8-DOX complexes. We note that all animal experiments were conducted using protocols approved by the Institutional Animal Care and Use Committee of Peking University. The photothermal effect of the AuNR@ZIF-8 core–shell nanostructures *in vivo* was assessed by infrared thermal imaging of tumor-bearing mice after intravenous injection (Fig. 5(a)). Upon NIR laser irradiation at 808 nm, the local surface temperature of tumors treated with the AuNR@ZIF-8 core–shell nanostructures increased steadily with prolonged irradiation time. The temperature could be elevated from 36.2 to 52.4 ℃ within 4 min at 1 $W \cdot cm^{-2}$. In comparison, the tumor treated with PBS only reached 34.8 ℃. The $4T_1$ tumor-bearing mice (tumor size of ~ 100 mm^3) were randomly divided into 8 groups with treatments of PBS, DOX, AuNR@ZIF-8 core–shell nanostructures, and AuNR@ZIF-8-DOX complexes via intravenous injection with or without NIR laser irradiation (Fig. 5(c)). In order to exert better therapy of the nanocarriers at the tumor site, both groups incubated with the AuNR@ZIF-8 core–shell nanostructures and AuNR@ZIF-8-DOX complexes under continuous NIR laser irradiation were first treated at ~ 42 ℃ for 10 min (Fig. S12 in the ESM) [67, 68], followed by 20 min of treatment at ~ 50 ℃ by adjusting the power of the NIR laser. Within a subsequent 14 days of monitoring, no statistically significant changes in body weight were found among all the groups (Fig. 5(b)), indicating the low systemic toxicity of both AuNR@ZIF-8 core–shell nanostructures and AuNR@ZIF-8-DOX complexes. After that, the mice were sacrificed and the tumors were excised and weighed to evaluate the tumor inhibition rates (Figs. 5(c), 5(d), and Fig. S13 in the ESM). Very impressively, the mice injected with AuNR@ZIF-8-DOX complexes under NIR irradiation exhibited the highest tumor suppression of about 90%, in comparison to the AuNR@ZIF-8 core–shell nanostructures with NIR irradiation (~ 58%) and the AuNR@ZIF-8-DOX complexes without NIR irradiation (~ 30%), disclosing the obvious effective synergy between photothermal therapy and chemotherapy *in vivo*. Moreover, no noticeable weight change was discerned in the major organs (heart, liver, lung, and kidney) except for the spleen (Fig. S14 in the ESM). Since the enlargement of the spleen is a typical syndrome in animals suffering from tumors [69], observation of the lightest spleen weight after treatment with AuNR@ZIF-8-DOX complexes under NIR irradiation manifested the best therapeutic effect by integrated photothermal therapy and chemotherapy.

The corresponding histological assessment demonstrated no damage or inflammation in the major organs

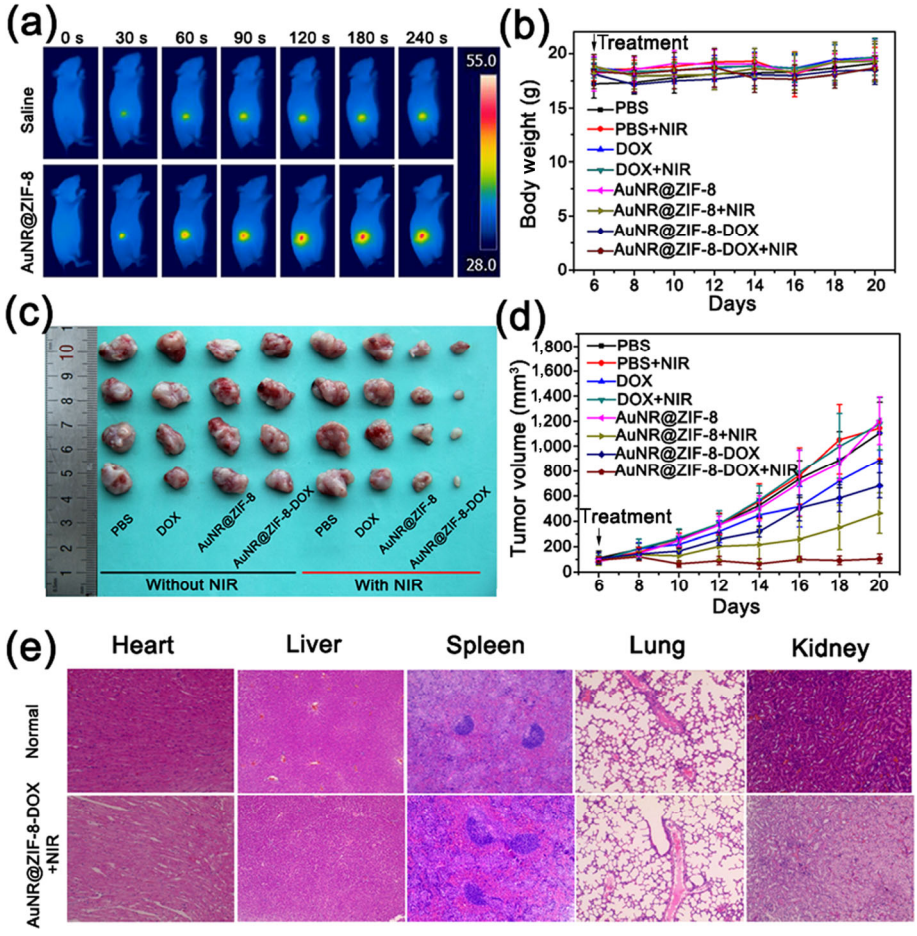

Figure 5 (a) *In vivo* infrared thermal images of $4T_1$ tumor-bearing mice after injection of either AuNR@ZIF-8 core–shell nanostructures or saline with different irradiation times under NIR laser at 808 nm (1 W·cm^{-2}); (b) and (d) observation of changes in (b) body weight and (d) relative tumor volume from $4T_1$ tumor-bearing mice with different treatments; (c) representative photograph of excised tumors from euthanized mice; (e) representative hematoxylin- and eosin-stained images of major tissues from mice after treatment. Magnification = 20× for heart, liver, spleen, lung, and kidney.

(Fig. 5(e) and Fig. S15 in the ESM), and blood biochemical markers were also maintained within the normal range (Table S3 in the ESM), well indicating their excellent biocompatibility and faint effects for cancer therapy.

In summary, in combination with the unique photothermal property of the AuNR cores and the remarkable drug-loading capacity and intrinsic responsive degradation of the ZIF-8 shells, the AuNR@ZIF-8 core–shell nanostructures exhibited controllable photothermal effect. Furthermore, with the high loading of DOX, the nanostructures easily realized pH and NIR dual stimuli-responsive drug release. Both *in vitro* and *in vivo* anticancer experiments confirmed that the AuNR@ZIF-8-DOX complexes under NIR laser irradiation at 808 nm possessed the highest toxicity at cellular and animal levels compared with single therapeutic treatment such as chemotherapy and photothermal therapy, indicating the outstanding synergistic effect of combined chemo-photothermal cancer therapy. Notably, both the acidic environment of cancer tumor cells and the localized NIR-light-converted heat distribution greatly benefited in triggering the breakage of coordination bonds either between DOX and ZIF-8 shells or between Zn^{2+} and imidazolate in the ZIF-8 shell itself, resulting in good biodegradation of this multimodal system based on the AuNR@ZIF-8-DOX complexes.

All results including low systemic toxicity, remarkable biocompatibility, double staining of cell therapy, and tumor ablation via intravenous injection highlight this new type of core–shell noble metal@MOF nanostructure as an intriguing multifunctional nanoplatform for cancer ablation. It is worth stressing that compared to conventional core–shell nanocarriers of silica or polymer shells, the AuNR@ZIF-8 core–shell nanostructures themselves exhibit excellent response to stimuli and good biocompatibility without the need for tedious synthesis and postmodification. Thanks to the well-established synthesis strategies of both inorganic NPs and MOFs of varied compositions, structures, and shapes, it is expected that this work will open the door towards the creation of multifunctional NP@MOF composite nanostructures for high-performance and low-toxicity theranostics.

Acknowledgements

This work was supported financially by National Basic Research Program of China (Nos. 2014CB93-1801 and 2016YFA0200700, Z. Y. T.), National Natural Science Foundation for Distinguished Youth Scholars of China (No. 11425520, C. Y. C.), National Natural Science Foundation of China (Nos. 21721002, 21475029, and 91427302, Z. Y. T.; 21722301 and 21371038, Y. L. L.), Frontier Science Key Project of the Chinese Academy of Sciences (No. QYZDJ-SSW-SLH038, Z. Y. T.), CAS-CSIRO Cooperative Research Program (No. GJHZ1503, Z. Y. T.), "Strategic Priority Research Program" of Chinese Academy of Sciences (No. XDA09040100, Z. Y. T.; XDA09030308, Y. L. L.), Youth Innovation Promotion Association of Chinese Academy of Sciences (Y. L. L.), and K. C. Wong Education Foundation (Z. Y. T.).

Electronic Supplementary Material: Supplementary material (detailed materials and methods, and additional experimental data) is available in the online version of this article at https://doi.org/10.1007/s122-74-017-1874-y.

References

[1] Ferrari, M. Cancer nanotechnology: Opportunities and challenges. *Nat. Rev. Cancer* **2005**, *5*, 161–171.

[2] Zhang, F. Y.; Shan, L.; Liu, Y. Y.; Neville, D.; Woo, J. H.; Chen, Y.; Korotcov, A.; Lin, S.; Huang, S.; Sridhar, R. et al. An anti-PSMA bivalent immunotoxin exhibits specificity and efficacy for prostate cancer imaging and therapy. *Adv. Healthcare Mater.* **2013**, *2*, 736–744.

[3] Chen, G. Y.; Roy, I.; Yang, C. H.; Prasad, P. N. Nanochemistry and nanomedicine for nanoparticle-based diagnostics and therapy. *Chem. Rev.* **2016**, *116*, 2826–2885.

[4] Probst, C. E.; Zrazhevskiy, P.; Bagalkot, V.; Gao, X. H. Quantum dots as a platform for nanoparticle drug delivery vehicle design. *Adv. Drug Deliv. Rev.* **2013**, *65*, 703–718.

[5] Lim, E. K.; Kim, T.; Paik, S.; Haam, S.; Huh, Y. M.; Lee, K. Nanomaterials for theranostics: Recent advances and future challenges. *Chem. Rev.* **2015**, *115*, 327–394.

[6] Liang, C.; Xu, L. G.; Song, G. S.; Liu, Z. Emerging nanomedicine approaches fighting tumor metastasis: Animal models, metastasis-targeted drug delivery, phototherapy, and immunotherapy. *Chem. Soc. Rev.* **2016**, *45*, 6250–6269.

[7] Elsabahy, M.; Wooley, K. L. Design of polymeric nanoparticles for biomedical delivery applications. *Chem. Soc. Rev.* **2012**, *41*, 2545–2561.

[8] Kemp, J. A.; Shim, M. S.; Heo, C. Y.; Kwon, Y. J. "Combo" nanomedicine: Co-delivery of multi-modal therapeutics for efficient, targeted, and safe cancer therapy. *Adv. Drug Deliv. Rev.* **2016**, *98*, 3–18.

[9] Cheng, L.; Wang, C.; Feng, L. Z.; Yang, K.; Liu, Z. Functional nanomaterials for phototherapies of cancer. *Chem. Rev.* **2014**, *114*, 10869–10939.

[10] Elsabahy, M.; Heo, G. S.; Lim, S. M.; Sun, G. R.; Wooley, K. L. Polymeric nanostructures for imaging and therapy. *Chem. Rev.* **2015**, *115*, 10967–11011.

[11] Yang, X.; Yang, M. X.; Pang, B.; Vara, M.; Xia, Y. N. Gold nanomaterials at work in biomedicine. *Chem. Rev.* **2015**, *115*, 10410–10488.

[12] Moon, G. D.; Choi, S. W.; Cai, X.; Li, W. Y.; Cho, E. C.; Jeong, U.; Wang, L. V.; Xia, Y. N. A new theranostic system based on gold nanocages and phase-change materials with unique features for photoacoustic imaging and controlled release. *J. Am. Chem. Soc.* **2011**, *133*, 4762–4765.

[13] Liu, Y. J.; He, J.; Yang, K. K.; Yi, C. L.; Liu, Y.; Nie, L. M.; Khashab, N. M.; Chen, X. Y.; Nie, Z. H. Folding up of gold nanoparticles strings into plasmonic vesicles for enhanced photoacoustic imaging. *Angew. Chem., Int. Ed.* **2015**, *54*, 15809–15812.

[14] Cui, T.; Liang, J. J.; Chen, H.; Geng, D. D.; Jiao, L.; Yang, J. Y.; Qian, H.; Zhang, C.; Ding, Y. Performance of doxorubicin-conjugated gold nanoparticles: Regulation of drug location. *ACS Appl. Mater. Interfaces* **2017**, *9*, 8569–8580.

[15] Chen, H. J.; Shao, L.; Li, Q.; Wang, J. F. Gold nanorods and their plasmonic properties. *Chem. Soc. Rev.* **2013**, *42*, 2679–2724.

[16] Lucky, S. S.; Soo, K. C.; Zhang, Y. Nanoparticles in Photodynamic therapy. *Chem. Rev.* **2015**, *115*, 1990–2042.

[17] You, J.; Shao, R. P.; Wei, X.; Gupta, S.; Li, C. Near-infrared light triggers release of paclitaxel from biodegradable microspheres: Photothermal effect and enhanced antitumor activity. *Small* **2010**, *6*, 1022–1031.

[18] Li, W.; Zhang, X. J.; Zhou, M. J.; Tian, B. S.; Yu, C. Y.; Jie, J. S.; Hao, X. J.; Zhang, X. H. Functional core/shell drug nanoparticles for highly effective synergistic cancer therapy. *Adv. Healthcare Mater.* **2014**, *3*, 1475–1485.

[19] Wu, G. H.; Mikhailovsky, A.; Khant, H. A.; Fu, C.; Chiu, W.; Zasadzinski, J. A. Remotely triggered liposome release by near-infrared light absorption *via* hollow gold nanoshells. *J. Am. Chem. Soc*. **2008**, *130*, 8175–8177.

[20] Yavuz, M. S.; Cheng, Y. Y.; Chen, J. Y.; Cobley, C. M.; Zhang, Q.; Rycenga, M.; Xie, J. W.; Kim, C. H.; Song, K. H.; Schwartz, A. G. et al. Gold nanocages covered by smart polymers for controlled release with near-infrared light. *Nat. Mater*. **2009**, *8*, 935–939.

[21] Zhang, Z. J.; Wang, L. M.; Wang, J.; Jiang, X. M.; Li, X. H.; Hu, Z. J.; Ji, Y. L.; Wu, X. C.; Chen, C. Y. Mesoporous silica-coated gold nanorods as a light-mediated multifunctional theranostic platform for cancer treatment. *Adv. Mater*. **2012**, *24*, 1418–1423.

[22] Croissant, J.; Zink, J. I. Nanovalve-controlled cargo release activated by plasmonic heating. *J. Am. Chem. Soc.* **2012**, *134*, 7628–7631.

[23] Wang, S. Z.; McGuik, C. M.; Ross, M. B.; Wang, S. Y.; Chen, P. C.; Xing, H.; Liu, Y.; Mirkin, C. A. General and direct method for preparing oligonucleotide-functionalized metal-organic framework nanoparticles. *J. Am. Chem. Soc.* **2017**, *139*, 9827–9830.

[24] Horcajada, P.; Gref, R.; Baati, T.; Allan, P. K.; Maurin, G.; Couvreur, P.; Férey, G.; Morris, R. E.; Serre, C. Metal-organic frameworks in biomedicine. *Chem. Rev.* **2012**, *112*, 1232–1268.

[25] He, C. B.; Liu, D. M.; Lin, W. B. Nanomedicine applications of hybrid nanomaterials built from metal-ligand coordination bonds: Nanoscale metal-organic frameworks and nanoscale coordination polymers. *Chem. Rev.* **2015**, *115*, 11079–11108.

[26] Wang, H. S.; Li, J.; Li, J. Y.; Wang, K.; Ding, Y.; Xia, X. H. Lanthanide-based metal-organic framework nanosheets with unique fluorescence quenching properties for two-color intracellular adenosine imaging in living cells. *NPG Asia Mater.* **2017**, *9*, e354.

[27] Horcajada, P.; Serre, C.; Maurin, G.; Ramsahye, N. A.; Balas, F.; Vallet-Regí, M.; Sebban, M.; Taulelle, F.; Férey, G. Flexible porous metal-organic frameworks for a controlled drug delivery. *J. Am. Chem. Soc.* **2008**, *130*, 6774–6780.

[28] Horcajada, P.; Chalati, T.; Serre, C.; Gillet, B.; Sebrie, C.; Baati, T.; Eubank, J. F.; Heurtaux, D.; Clayette, P.; Kreuz, C. et al. Porous metal-organic-framework nanoscale carriers as a potential platform for drug delivery and imaging. *Nat. Mater.* **2010**, *9*, 172–178.

[29] Cai, G. R.; Jiang, H. L. A modulator-induced defect-formation strategy to hierarchically porous metal-organic frameworks with high stability. *Angew. Chem., Int. Ed.* **2017**, *56*, 563–567.

[30] An, J.; Geib, S. J.; Rosi, N. L. Cation-triggered drug release from a porous zinc-adeninate metal-organic framework. *J. Am. Chem. Soc*. **2009**, *131*, 8376–8377.

[31] Wang, W. Q.; Wang, L.; Li, Z. S.; Xie, Z. G. BODIPY-containing nanoscale metal-organic frameworks for photodynamic therapy. *Chem. Commun.* **2016**, *52*, 5402–5405.

[32] Yang, Y. Y.; Hu, Q.; Zhang, Q.; Jiang, K.; Lin, W. X.; Yang, Y.; Cui; Y. J.; Qian, G. D. A large capacity cationic metal-organic framework nanocarrier for physiological pH responsive drug delivery. *Mol. Pharmaceutics* **2016**, *13*, 2782–2786.

[33] Zheng, H. Q.; Zhang, Y. N.; Liu, L. F.; Wan, W.; Guo, P.; Nyström, A. M.; Zou, X. D. One-pot synthesis of metal-organic frameworks with encapsulated target molecules and their applications for controlled drug delivery. *J. Am. Chem. Soc.* **2016**, *138*, 962–968.

[34] Wang, W. Q.; Wang, L.; Li, Y.; Liu, S.; Xie, Z. G.; Jing, X. B. Nanoscale polymer metal-organic framework hybrids for effective photothermal therapy of colon cancer. *Adv. Mater.* **2016**, *28*, 9320–9325.

[35] Zheng, X. H.; Wang, L.; Pei, Q.; He, S. S.; Liu, S.; Xie, Z. G. Metal-organic framework@porous organic polymer nanocomposite for photodynamic therapy. *Chem. Mater.* **2017**, *29*, 2374–2381.

[36] Lu, G.; Li, S. Z.; Guo, Z.; Farha, O. K.; Hauser, B. G.; Qi, X. Y.; Wang, Y.; Wang, X.; Han, S. Y.; Liu, X. G. et al. Imparting functionality to a metal-organic framework material by controlled nanoparticle encapsulation. *Nat. Chem*. **2012**, *4*, 310–316.

[37] Sun, C. Y.; Qin, C.; Wang, X. L.; Yang, G. S.; Shao, K. Z.; Lan, Y. Q.; Su, Z. M.; Huang, P.; Wang, C. G.; Wang, E. B. Zeolitic imidazolate framework-8 as efficient pH-sensitive drug delivery vehicle. *Dalton Trans*. **2012**, *41*, 6906–6909.

[38] Ren, H.; Zhang, L. Y.; An, J. P.; Wang, T. T.; Li, L.; Si, X. Y.; He, L.; Wu, X. T.; Wang, C. G.; Su, Z. M. Polyacrylic acid@zeolitic imidazolate framework-8 nanoparticles with ultrahigh drug loading capability for pH-sensitive drug release. *Chem. Commun.* **2014**, *50*, 1000–1002.

[39] Wang, Z. F.; Tang, X. J.; Wang X. X.; Yang, D. D.; Yang, C.; Lou, Y. B.; Chen, J. X.; He, N. Y. Near-infrared light-induced dissociation of zeolitic imidazole framework-8 (ZIF-8) with encapsulated CuS nanoparticles and their application as a therapeutic nanoplatform. *Chem. Commun*. **2016**, *52*, 12210–12213.

[40] Tian, Z. F.; Yao, X. X.; Ma, K. X.; Niu, X. X.; Grothe, J. L.; Xu, Q. N.; Liu, L. S.; Kaskel, S.; Zhu, Y. F. Metal-organic framework/graphene quantum dot nanoparticles used for synergistic chemo- and photothermal therapy. *ACS Omega* **2017**, *2*, 1249–1258.

[41] Dykman, L.; Khlebtsov, N. Gold nanoparticles in biomedical applications: Recent advances and perspectives. *Chem. Soc. Rev*. **2012**, *41*, 2256–2282.

[42] Cobley, C. M.; Chen, J. Y.; Cho, E. C.; Wang, L. V.; Xia, Y. N. Gold nanostructures: A class of multifunctional materials for biomedical applications. *Chem. Soc. Rev.* **2011**, *40*, 44–56.

[43] Nikoobakht, B.; El-Sayed, M. A. Preparation and growth mechanism of gold nanorods (NRs) using seed-mediated

growth method. *Chem. Mater.* **2003**, *15*, 1957–1962.

[44] He, L. C.; Liu, Y.; Liu, J. Z.; Xiong, Y. S.; Zheng, J. Z.; Liu, Y. L.; Tang, Z. Y. Core-shell noble-metal@metal-organic-framework nanoparticles with highly selective sensing property. *Angew. Chem., Int. Ed.* **2013**, *52*, 3741–3745.

[45] Liu, X.; He, L. C.; Zheng, J. Z.; Guo, J.; Bi, F.; Ma, X.; Zhao, K.; Liu, Y. L.; Song, R.; Tang, Z. Y. Solar-light-driven renewable butanol separation by core-shell Ag@ZIF-8 nanowires. *Adv. Mater.* **2015**, *27*, 3273–3277.

[46] Li, Y. T.; Tang, J. L.; He, L. C.; Liu, Y.; Liu, Y. L.; Chen, C. Y.; Tang, Z. Y. Core-shell upconversion nanoparticle@metal-organic framework nanoprobes for luminescent/magnetic dual-mode targeted imaging. *Adv. Mater.* **2015**, *27*, 4075–4080.

[47] Hayashi, H.; Côté, A. P.; Furukawa, H.; O'Keeffe, M.; Yaghi, O. M. Zeolite a imidazolate frameworks. *Nat. Mater.* **2007**, *6*, 501–506.

[48] Abraham, S. A.; Edwards, K.; Karlsson, G.; MacIntosh, S.; Mayer, L. D.; McKenzie, C.; Bally, M. B. Formation of transition metal-doxorubicin complexes inside liposomes. *Biochim. Biophys. Acta, Biomembr*. **2002**, *1565*, 41–54.

[49] Barick, K. C.; Nigam S.; Bahadur, D. Nanoscale assembly of mesoporous ZnO: A potential drug carrier. *J. Mater. Chem.* **2010**, *20*, 6446–6452.

[50] Vasconcelos, I. B.; da Silva, T. G.; Militão, G. C. G.; Soares, T. A.; Rodrigues, N. M.; Rodrigues, M. O.; da Costa, N. B., Jr.; Freire, R. O.; Junior, S. A. Cytotoxicity and slow release of the anti-cancer drug doxorubicin from ZIF-8. *RSC Adv.* **2012**, *2*, 9437–9442.

[51] Yang, J. P.; Shen, D. K.; Zhou, L.; Li, W.; Li, X. M.; Yao, C.; Wang, R.; El-Toni, A. M.; Zhang, F.; Zhao, D. Y. Spatially confine fabrication of core-shell gold nanocages@-mesoporous silica for near-infrared controlled photothermal drug release. *Chem. Mater.* **2013**, *25*, 3030–3037.

[52] Zhang, L. Y.; Chen, Y. Y.; Li, Z. L.; Li, L.; Saint-Cricq, P.; Li, C. X.; Lin, J.; Wang, C. G.; Su, Z. M.; Zink, J. I. Tailored synthesis of octopus-type janus nanoparticles for synergistic actively-targeted and chemo-photothermal therapy. *Angew. Chem., Int. Ed*. **2016**, *55*, 2118–2121.

[53] Chen, R.; Zhang, J. F.; Wang, Y.; Chen, X. F.; Zapien, J. A.; Lee, C. S. Graphitic carbon nitride nanosheet@metal-organic framework core-shell nanoparticles for photo-chemo combination therapy. *Nanoscale* **2015**, *7*, 17299–17305.

[54] Chen, X. J.; Zhang, M. J.; Li, S. N.; Li, L.; Zhang, L. Y.; Wang, T. T.; Yu, M.; Mou, Z. C.; Wang, C. G. Facile synthesis of polypyrrole@metal-organic framework core-shell nanocomposites for dual-mode imaging and synergistic chemo-photothermal therapy of cancer cells. *J. Mater. Chem. B* **2017**, *5*, 1772–1778.

[55] Ke, F.; Yuan, Y. P.; Qiu, L. G.; Shen, Y. H.; Xie, A. J.; Zhu, J. F.; Tian, X. Y.; Zhang, L. D. Facile fabrication of magnetic metal-organic framework nanocomposites for potential targeted drug delivery. *J. Mater. Chem*. **2011**, *21*, 3843–3848.

[56] Zhang, F. M.; Dong, H.; Zhang, X.; Sun, X. J.; Liu, M.; Yang, D. D.; Liu, X.; Wei, J. Z. Postsynthetic modification of ZIF-90 for potential targeted codelivery of two anticancer drugs. *ACS Appl. Mater. Interfaces* **2017**, *9*, 27332–27337.

[57] Zheng, H. Q.; Xing, L.; Cao, Y. Y.; Che, S. A. Coordination bonding based pH-responsive drug delivery systems. *Coord. Chem. Rev.* **2013**, *257*, 1933–1944.

[58] He, M. N.; Zhou, J. J.; Chen, J.; Zheng, F. C.; Wang, D. D.; Shi, R. H.; Guo, Z.; Wang, H. B.; Chen, Q. W. Fe_3O_4@carbon@zeolitic imidazolate framework-8 nanoparticles as multifunctional pH-responsive drug delivery vehicles for tumor therapy *in vivo*. *J. Mater. Chem. B* **2015**, *3*, 9033–9042.

[59] Park, K. S.; Ni, Z.; Côté, A. P.; Choi, J. Y.; Huang, R. D.; Uribe-Romo, F. J.; Chae, H. K.; Keeffe, M. O.; Yaghi, O. M. Exceptional chemical and thermal stability of zeolitic imidazolate frameworks. *Proc. Natl. Acad. Sci. USA* **2006**, *103*, 10186–10191.

[60] Fang, W. J.; Yang, J.; Gong, J. W.; Zheng, N. F. Photo- and pH-triggered release of anticancer drugs from mesoporous silica-coated Pd@Ag nanoparticles. *Adv. Funct. Mater*. **2012**, *22*, 842–848.

[61] Zhang, X. L.; Jiang, J. W. Thermal conductivity of zeolitic imidazolate framework-8: A molecular simulation study. *J. Phys. Chem. C* **2013**, *117*, 18441–18447.

[62] Sassaroli, E.; Li, K. C. P.; O'Neill, B. E. Numerical investigation of heating of a gold nanoparticle and the surrounding microenvironment by nanosecond laser pulses for nanomedicine applications. *Phys. Med. Biol*. **2009**, *54*, 5541–5560.

[63] Baffou, G.; Girard, C.; Quidant, R. Mapping heat origin in plasmonic structures. *Phys. Rev. Lett*. **2010**, *104*, 136805.

[64] Baffou, G.; Quidant, R.; de Abajo, F. J. G. Nanoscale control of optical heating in complex plasmonic systems. *ACS Nano* **2010**, *4*, 709–716.

[65] Lv, R. C.; Yang, P. P.; He, F.; Gai, S. L.; Li, C. X.; Dai, Y. L.; Yang, G. X.; Lin, J. A yolk-like multifunctional platform for multimodal imaging and synergistic therapy triggered by a single near-infrared light. *ACS Nano* **2015**, *9*, 1630–1647.

[66] Wang, Y.; Wang, K. Y.; Zhang, R.; Liu, X. G.; Yan, X. Y.; Wang, J. X.; Wagner, E.; Huang, R. Q. Synthesis of core–shell graphitic carbon@silica nanospheres with dual-ordered mesopores for cancer-targeted photothermochemotherapy. *ACS Nano* **2014**, *8*, 7870–7879.

[67] Kirui, D. K.; Celia, C.; Molinaro, R.; Bansal, S. S.; Cosco, D.; Fresta, M.; Shen, H. F.; Ferrari, M. Mild hyperthermia enhances transport of liposomal gemcitabine and improves *in vivo* therapeutic response. *Adv. Healthcare Mater.* **2015**, *4*, 1092–1103.

[68] Kirui, D. K.; Koay, E. J.; Guo, X. J.; Cristini, V.; Shen, H. F.; Ferrari, M. Tumor vascular permeabilization using localized mild hyperthermia to improve macromolecule transport. *Nanomedicine* **2014**, *10*, 1487–1496.

[69] Chae, W. J.; Gibson, T. F.; Zelterman, D.; Hao, L. M.; Henegariu, O.; Bothwell, A. L. M. Ablation of IL-17A abrogates progression of spontaneous intestinal tumorigenesis. *Proc. Natl. Acad. Sci. USA* **2010**, *107*, 5540–5544.